Tuning the Electronic and Transport Properties of Three Configurations of Penta-Graphene Nanoribbons

M. Balvasi, A. Avazpour*,
J. Jalilian and M.Z. Bidsardare

Physics Department, Faculty of Science, Yasouj University, Yasouj, Iran

Received: 12.06.2023 & Accepted: 05.09.2023

Doi: 10.12693/APhysPolA.144.214 *e-mail: avazpour@yu.ac.ir

We investigated the effects of the strain, edges, and width of penta-graphene nanoribbons on their electronic structure and transport properties using tight-binding approximation. We considered three different geometries of penta-graphene nanoribbons. In the first case, both the upper and lower edges have a zigzag shape. In the second case, the upper edge has a zigzag pattern, and the lower edge has a beard shape. In the third case, both the upper and lower edges are considered to be beard-shaped. The hopping parameters were evaluated based on Slater–Koster integrals. The Slater–Koster coefficients were evaluated using the TBStudio software package. In our model, we do not apply arbitrary amounts of strain to the structure. For the stability of the structure, we chose the allowable amounts of strain by using the calculated strain–stress curve. Based on the tight-binding approximation, the magnitude of the bandgap in each type of penta-graphene nanoribbon is reduced as the applied strain increases. In addition, the band structures of the three geometries changed, and the bandgap decreased with an increase in width. Hence, such configurations of penta-graphene nanoribbons are expected to be widely used in nano-electronic devices. Finally, we investigated transport properties using a tight-binding model and a generalized Green's function method in the Landauer–Buttiker formalism. By tuning the width of the penta-graphene nanoribbons and applying strain, the maximum current and a lower threshold voltage are achieved. With an increase in the width of the nanoribbon, the intensity of the current and the available energy levels have increased. Our calculated results may suggest potential applications of penta-graphene nanoribbons in spin electronics, nano-electronic devices, and solar cells. In addition, we provide theoretical guidance for regulating the properties of penta-graphene nanoribbons by applying strain, edge modifications, and different widths.

topics: penta-graphene nanoribbon, tight-binding approximation, electronic and transport properties, strain and edge modifications

1. Introduction

In the last two decades, there has been a dramatic surge in the study of two-dimensional (2D) crystalline materials. The first realized 2D material, an isolated single layer of carbon hexagons consisting of SP_2 hybridized carbon–carbon bonding with P_z-electrons, called graphene, has a number of unique properties that make it interesting for both fundamental studies and future applications [1]. Despite its remarkable properties, it has a major drawback — the intrinsic zero bandgap in the pristine graphene [1–3] that hinders its applications and performance in electronic and optoelectronic devices [4] and sparks the search for other 2D materials with desirable properties. Accordingly, the issue of producing a controllable and tunable bandgap in graphene-based materials without degrading their high carrier mobility has attracted intense attention for applications in visible optoelectronic elements. Beyond the already synthesized hexagonal 2D materials, such as transition metal dichalcogenides (TMDCs) [5–8], the hexagonal boron nitride (h-BN) [9], borophene [10–12], silicone [13, 14], phosphorene [15–17], and MXenes [18, 19], there are many of 2D materials with promising properties being proposed theoretically [20, 21].

Hexagons are the most common building blocks in the atomic structures of these existing and predicted 2D materials, which share a similar hexagonal lattice to graphene. The unique features of these materials are attributed to their hexagonal symmetries. In 2015, a new 2D carbon allotrope with a pentagonal structure resembling the Cairo pentagonal tiling was reported by Zhang et al. [22]. State-of-the-art theoretical calculations along with

a combination of first-principles calculations confirmed that the new carbon polymorph is dynamically and mechanically stable and can withstand temperatures as high as 1000 K. Since the penta-graphene (PG) prediction, there have been many theoretical and experimental studies exploring the applicability and development of new pentagonal materials with qualities superior to the existing ones, including hydrogenated PG [23], penta-$PdSe_2$ [24–26], penta-BN_2 [27], penta-Pt_2N_4 [28], penta-AgN_3 [29], penta-SiC_2 [30], penta-CN_2 [31], TiC_2 [32], $PdSe_2$ [24], and penta-silicene nanoribbons [33]. Recently, stable penta-silicene was found by reducing the Coulomb interaction of silicon dimers [34]. This first pentagonal arrangement of carbon atoms, a structure that contains both SP_3-like and SP_2-like hybridizations of carbon bonds, is called penta-graphene (PG) [22, 35–38], and its prototype was first proposed in iron-based structures with exotic magnetic frustration [39].

Penta-graphene is known to possess several unique characteristics, including (i) reduced thermal conductivity compared to graphene [40–42], (ii) unusual in-plane negative Poisson ratio [22, 43] due to the Coulombic repulsion between the nearby SP_3 bonds caused by the tetrahedral character of the SP_3-like hybridization, ultrahigh ideal strength outperforming graphene, and other interesting electronic properties [22, 44], which make it a potential candidate for wide applications in optoelectronic and photovoltaic devices. Its room-temperature thermal conductivity is about 167 W/(m K) [44], which is much lower than that of graphene (above 3000 W/(m K) [45]). Additionally, (iii) penta-graphene is a semiconductor presenting bandgap values of about 2.24–4.3 eV [22, 46], which makes it attractive for optoelectronic applications that have no need to functionalize PG for opening the bandgap as is the case with graphene. (iv) Regardless of its chirality, the 2D PG can be rolled up to form a one-dimensional semiconducting pentagon-based nanotube. Meanwhile, as the PG surface is not precisely flat, it has a higher chance for the adsorption of adsorbing molecules, which broadens the options for using PG as an active layer in novel sensor prototypes [22] and gas sensor applications [47].

On the one hand, in order to be integrated into planar circuitry, either graphene or other carbon allotropes should be used as nanoribbons with controlled width and precise spatial arrangement. Thus, converting 2D materials into one-dimensional (1D) nanoribbons has been of both fundamental and technological interest during the past two decades because of the interesting electronic and physical properties intrinsically associated with their low dimensionality and quantum confinement effect. On the other hand, tuning the physical properties of nanoribbons by external fields is an important issue for using these materials in various applications in the nanoscience and/or nanotechnology

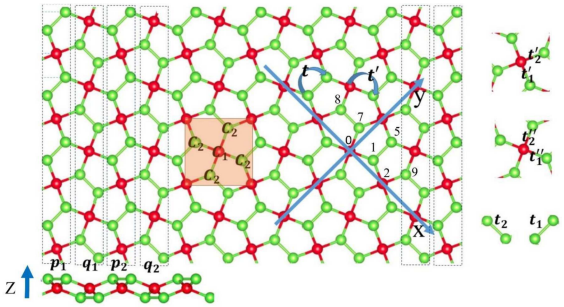

Fig. 1. Top and side views of the PG lattice. The unit cell comprising 6 carbon atoms is enclosed in a black square. Atoms with coordination number 4 are labeled as C_1, those with coordination number 3 are labeled as C_2; here t_1', t_2', t_1'', t_2'', t_1, and t_2 are hopping parameters after applying strain, while t and t' — hopping parameters before applying strain.

communities. The large bandgap of PG suggests the need to develop gap-tuning strategies to tailor this material for optoelectronic applications. Various experimental and theoretical approaches have been proposed in this field. Applying a staggered sublattice potential and strain are two important ways to achieve such tuning. The tuning of the electronic properties of materials is at the heart of modern electronics. Strain engineering, as an efficient strategy to tune the electronic properties of materials and explore new quantum states in condensed matter physics, gives rise to an emerging research field referred to as "straintronics" [48] that lies at the heart of modern electronics in atomically thin materials. Strain engineering is also a key strategy for manipulating the magnetic coupling in 2D nanostructures [49]. Motivated by the search for materials for spintronics, many studies have been performed to examine the effectiveness of mechanical strain in modulating the magnetic properties of 2D layered materials [49, 50].

In this study, the effects of uniaxial strain, edges, and width on the electronic structure and transport properties of three configurations of penta-graphene nanoribbons (PGNRs) were studied using tight-binding approximation (TBA) and nonequilibrium Green's function (NEGF) formalism. Using the calculated strain–stress curve, the allowable amounts of strain were applied. This study paves the way for the design and fabrication of PG-based electronic devices.

2. Structure

The atomic configuration of PG is shown in Fig. 1. The optimized crystal structure of the 2D pentagon-based phase was generated by exfoliating a single layer of T12-carbon. The structure possesses $P42_1m$ symmetry (space group no. 113)

with a tetragonal lattice. The optimized lattice constants are $a = b = 3.64$ Å. The PG lattice exhibited a small buckling thickness (h) in the out-of-plane direction, in contrast to the planar structure of graphene. The top view shows that the new phase was composed entirely of carbon pentagons, forming a beautiful pattern known as Cairo pentagonal tiling. From the side view, buckling $h = 0.6$ Å is observed, leading to a 2D sheet with a total thickness of 1.20 Å. This structure has two hybridizations, i.e., SP_2 and SP_3. The Carbon atoms C_1 and C_2 in the unit cell have different coordination numbers owing to their different hybridizations. The SP_3 and SP_2 hybridizations are denoted as C_1 and C_2, respectively, where the C_1:C_2 ratio is 1:2. The bond length of a single bond (C_1–C_2) is 1.55 Å, and the bond length of the double bond (C_2–C_2) is 1.34 Å. The origin of the Cartesian coordinate system was chosen to be located on the red atom at the center of the unit cell, and the diameters of our penta-graphene structure were set to be along the x- and y-axes. The z-axis is in the direction normal to the PG plane, which will be chosen as atoms 1, 2, 5, 7, 8, and 9 in this work. The coordinates of these atoms are

$$\begin{aligned} \boldsymbol{r}_1 &= \left(\frac{\sqrt{3}}{2}, \frac{1}{2}, h\right), & \boldsymbol{r}_2 &= \left(\sqrt{3}, 0, 0\right), \\ \boldsymbol{r}_5 &= (0.86, 1.23, h), & \boldsymbol{r}_7 &= \left(-\frac{1}{2}, \frac{\sqrt{3}}{2}, -h\right), \\ \boldsymbol{r}_8 &= (-0.86, 1.23, -h), & \boldsymbol{r}_9 &= (2.08, 1.2, -h). \end{aligned} \tag{1}$$

3. Tight-binding approximation

One of the simplest methods for calculating the band structure of a material is tight-binding approximation (TBA). TBA has been available for electronic structure calculations since it was first proposed by Felix Bloch in 1928 [51]. Because it utilizes symmetries and semi-empirical formalism for parameters instead of explicit functions and exact forms, it often serves as an initial step in understanding the nature of electronic structures. A key point in TBA is the concept of localized orbitals. Wave functions are understood in terms of a linear combination of highly localized atomic orbitals. The unit cell in Fig. 1 is denoted by a square and consists of one C_1 atom and four C_2 atoms. Each C_1 atom in the unit cell is connected to the C_2 atom by the hopping parameter, t'. In addition, each C_2 atom is connected to its nearest neighboring C_2 atom using the hopping parameter t. The hopping parameters were evaluated based on Slater–Koster (SK) integrals. Using the TBStudio software package, the SK coefficients were evaluated [52] by fitting the band energies of the TB model to those of the first-principles calculations,

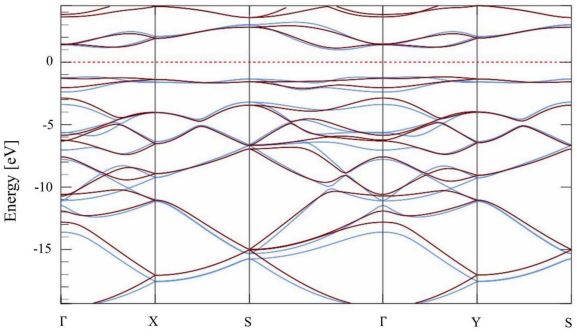

Fig. 2. Fit of PG energy band structures calculated with DFT (blue solid lines) and TB (crimson solid lines). There is a good agreement between them near the Fermi level.

TABLE I

Slater–Koster tight-binding parameters (in [eV]) for penta-graphen evaluated using TBStudio, where $E_S = -7.39$.

On-site energies of C [eV]		
$E_{Py} = 1.50$	$E_{Pz} = 1.13$	$E_{Px} = 1.23$
Hopping parameters		
Bond 1	Bond 2	Bond 3
$V_{SS\sigma} = -3.26$	$V_{SS\sigma} = -3.93$	$V_{SS\sigma} = -0.08$
$V_{SP\sigma} = 3.67$	$V_{SP\sigma} = 3.10$	$V_{SP\sigma} = -0.08$
$V_{PP\sigma} = 4.46$	$V_{PP\sigma} = 4.34$	$V_{PP\sigma} = 0.13$
$V_{PP\pi} = -2.06$	$V_{PP\pi} = -2.82$	$V_{PP\pi} = -0.18$

as shown in Fig. 2. First-principle calculations were carried out using OpenMX [53]. Thus, PG-based nanostructures, such as nanoribbons, can be described using this approach. The final TB parameter values are listed in Table I.

In this study, we considered only the nearest neighbors (see Fig. 3). Bond 1 (C_1–C_2 which is marked with red color), bond 2 (C_2–C_2 which is marked with green color), and, more specifically, the P_z orbitals of carbon atoms are considered because the frontier bands of penta-graphene (close to the Fermi level) are dominated by the P_z states of hybridized C atoms [54]. Also, the on-site energy values were considered to be the same for all carbon atoms.

The bond length and angle have been deformed by applying strain to the system. This implies that the initial hopping values (t and t') are changed. Therefore, as shown in Fig. 3, after applying strain, the PG structure has six hopping parameters: t_1, t_2, t_1', t_2', t_1'', and t_2''. Hence, we describe the electronic band structure of PG obtained using the TBA model. The tight-binding Hamiltonian for PGNR is [55–62]

$$H = \sum_{i,j} t_{i,j}\ c_i^\dagger c_j + \sum_i U_i\ c_i^\dagger c_i, \tag{2}$$

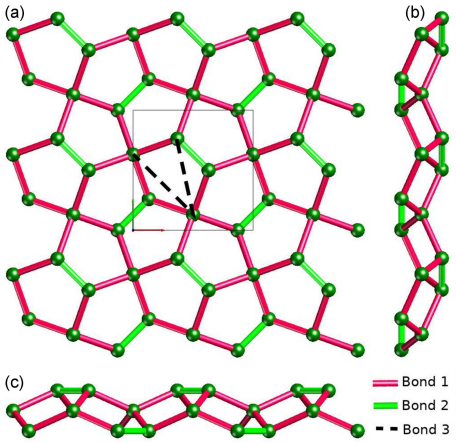

Fig. 3. (a) Top and (b, c) side views of the PG lattice. The black square indicates unit cell, the links shown in red (C_1–C_2) and green (C_2–C_2) are nearest neighbors. Also, the black dashed indicate next nearest neighbors.

where c_i^+ (c_j) is the creation (annihilation) operator of an electron on site i (j), $t_{i,j}$ is the hopping energy between sites i and j, and the summations run over all site-pairs with nonzero hopping. In (2), U_i is the on-site energy of the i-th atom. In this work, only nearest neighborhood hopping, including two types of intra-layer hopping and one type of inter-layer hopping, was considered. Using an accurate tight-binding model, the momentum space dispersion of a PG nanoribbon was directly calculated. We assumed a periodic boundary condition along the ribbon in the x-direction. Applying Bloch's theorem, performing the Fourier transformation along the x-direction, the Hamiltonian in $\boldsymbol{k}$ space can be written as [58–61]

$$H(k) = H_{00} + H_{01}\,\mathrm{e}^{-\mathrm{i}k_x a} + H_{01}^{\dagger}\,\mathrm{e}^{\mathrm{i}k_x a}, \tag{3}$$

where a is the unit-cell length along the x-axis. Also, H_{00} and H_{01} describe coupling within a principal unit cell (intra-unit cell) and between the adjacent principal unit cells (inter-unit cell), respectively, which can be mapped from the real space tight-binding model given by (2). Based on the TBA model, the electronic Hamiltonian for the PG in real space can be written as

$$H = \begin{pmatrix} H_{p_1p_1} & H_{p_1q1} & 0 & 0 \\ H_{q_1p_1} & H_{q_1q_1} & H_{q_1p_2} & 0 \\ 0 & H_{p_2q_1} & H_{p_2p_2} & H_{p_2q_2} \\ 0 & 0 & H_{q_2p_2} & H_{q_2q_2} \end{pmatrix}, \tag{4}$$

where $H_{p_ip_i(q_iq_i)}$ and $H_{p_iq_i(q_ip_i)}$ are the intra- and inter-unit cell $(M\times N)\times(M\times N)$ matrices, respectively.

We investigate the effects of strain, edges, and the width of penta-graphene nanoribbon (PGNR) on the electronic structure. We considered three different PGNR geometries. In the first case, both the upper and lower edges have a zigzag (ZZ) form. In the second case, the upper edge has a zigzag pattern, and the lower edge is beard-shaped (ZB). In the third case, both the upper and lower edges are considered to be beard-shaped (BB). For each of the above cases, we determined the Hamiltonian using the TBA method and investigated the effect of strain, edges, and width of the PGNR on the electronic structure. If the width of the NR is denoted by M, the allowable values for M in considered cases of ZZ, ZB, and BB are $M_n = 3n$, $M_n = a_1 + (n-1)d$, and $M_n = a_2 + (n-1)d$, respectively. Here, n is an integer, $d = 3$, $a_1 = 5$, and $a_2 = 4$.

4. Strain effect on electronic bandgap

4.1. General formula for strain modulated bandgap

We now consider the strain effect on the electronic bandgap of PG. The electronic bands for PG are composed of S and P orbitals [62]. Moreover, the hopping parameter between S and P orbitals depends on the bond length (r) as $t \propto 1/r^2$ [63–66]. The strain effect is realized by changing the bond length. Thus, the applied mechanical strain can affect electronic states (including the bandgap) by modifying the hopping parameters in the TBA model. We consider the deformation of PGNR under a general mechanical strain in the direction with angle ϕ. The direction angle ϕ is determined starting from the x-axis. We perform a coordinate transformation by rotating the x-axis in Fig. 1 to the strain direction $\hat{e}_\phi = \hat{e}_x\cos(\phi) + \hat{e}_y\sin(\phi)$. The coordinates for a vector in this new coordinate system become

$$\begin{pmatrix} x_\phi \\ y_\phi \\ z_\phi \end{pmatrix} = \begin{pmatrix} \cos(\phi) & \sin(\phi) & 0 \\ -\sin(\phi) & \cos(\phi) & 0 \\ 0 & 0 & 1 \end{pmatrix} \begin{pmatrix} x \\ y \\ z \end{pmatrix}, \tag{5}$$

where (x, y, z) is the original coordinate for the vector, and the subscript ϕ denotes quantities in the new coordinate system. In the new coordinate system, the coordinates are deformed by an arbitrary linear mechanical strain as follows

$$\begin{pmatrix} x_\varepsilon \\ y_\varepsilon \\ z_\varepsilon \end{pmatrix} = \begin{pmatrix} 1+\varepsilon_x & \gamma & 0 \\ \gamma & 1+\varepsilon_y & 0 \\ 0 & 0 & 1+\varepsilon_z \end{pmatrix} \begin{pmatrix} x_\phi \\ y_\phi \\ z_\phi \end{pmatrix}, \tag{6}$$

where γ is the shear component and is taken to be zero, and ε_x, ε_y, and ε_z are the normal strains. The subscript ε in the coordinates denotes the quantity after the deformation. In the linear deformation regime, the bond length r can be expanded as a function of all the strain components $\varepsilon_x, \varepsilon_y, \varepsilon_z$, and γ, as

$$r = r_0 + \frac{\partial r}{\partial \varepsilon_x}\varepsilon_x + \frac{\partial r}{\partial \varepsilon_y}\varepsilon_y + \frac{\partial r}{\partial \varepsilon_z}\varepsilon_z + \frac{\partial r}{\partial \gamma}\gamma \equiv$$

$$r_0 + \alpha_x\varepsilon_x + \alpha_y\varepsilon_y + \alpha_z\varepsilon_z + \alpha_s\gamma, \tag{7}$$

where we introduce α as the strain-related geometrical coefficient. Using the relation between the hopping parameter and bond length, the strain effect on the hopping parameter is

$$t_i = t_{i0}\left(1-\frac{2\,\alpha_{ix}\varepsilon_x}{r_0}-\frac{2\,\alpha_{iy}\varepsilon_y}{r_0}-\frac{2\,\alpha_{iz}\varepsilon_z}{r_0}-\frac{2\,\alpha_{is}\gamma}{r_0}\right). \tag{8}$$

According to (8), the key element is to compute the strain-related geometrical coefficients α for each hopping parameter; t_{i0} is the nearest neighbor hopping integral in the absence of strain ($t'_{10} = t'_{20} = t''_{10} = t''_{20} = t'$, $t_{10} = t_{20} = t$), and $r_{\rm o}$ is the unstrained structure bond length. For strain ε_x, we obtain the following geometrical coefficients for each hopping parameter t_i ,

$$\alpha_{ix} = \frac{\partial r_{jk}}{\partial \varepsilon_x}\bigg|_{\varepsilon_{x=0}} = \frac{1}{r_{jk}}x^2_{jk\phi} = \frac{1}{r_{jk}}\Big[(x_k-x_j)\cos(\phi)+(y_k-y_j)\sin(\phi)\Big]^2. \tag{9}$$

Here, α_{ix} is the coefficient corresponding to the hopping parameter t_i. For strain ε_y, we obtain the following geometrical coefficients

$$\alpha_{iy} = \frac{\partial r_{jk}}{\partial \varepsilon_y}\bigg|_{\varepsilon_{y=0}} = \frac{1}{r_{jk}}y^2_{jk\phi} = \frac{1}{r_{jk}}\Big[(x_j-x_k)\sin(\phi)+(y_k-y_j)\cos(\phi)\Big]^2. \tag{10}$$

Also, for the ε_z strain, the following geometrical coefficients are calculated

$$\alpha_{iz} = \frac{\partial r_{jk}}{\partial \varepsilon_z}\bigg|_{\varepsilon_{z=0}} = \frac{1}{r_{jk}}z^2_{jk\phi}. \tag{11}$$

Using (9)–(11), the modified forms of hopping parameters are represented as follows

$$\begin{aligned} r^x_{12} &= \frac{1}{r_{12}}\left[\frac{\sqrt{3}}{2}\cos(\phi)-\frac{1}{2}\sin(\phi)\right]^2,\\ r^y_{12} &= \frac{1}{r_{12}}\left[-\frac{\sqrt{3}}{2}\sin(\phi)-\frac{1}{2}\cos(\phi)\right]^2,\\ r^z_{12} &= -\frac{h^2}{r_{12}}, \end{aligned} \tag{12}$$

$$\begin{aligned} r^x_{29} &= \frac{1}{r_{29}}\Big[\Big(-\sqrt{3}{+}2.08\Big)\cos(\phi)+1.2\,\sin(\phi)\Big]^2,\\ r^y_{29} &= \frac{1}{r_{29}}\Big[\Big(\sqrt{3}{-}2.08\Big)\sin(\phi)+1.2\,\cos(\phi)\Big]^2,\\ r^z_{29} &= -\frac{h^2}{r_{29}}, \end{aligned} \tag{13}$$

$$\begin{aligned} r^x_{\rm o7} &= \frac{1}{r_{\rm o7}}\left[\frac{\sqrt{3}}{2}\sin(\phi)-\frac{1}{2}\cos(\phi)\right]^2,\\ r^y_{\rm o7} &= \frac{1}{r_{\rm o7}}\left[\frac{\sqrt{3}}{2}\cos(\phi)+\frac{1}{2}\sin(\phi)\right]^2,\\ r^z_{\rm o7} &= -\frac{h^2}{r_{\rm o7}}, \end{aligned} \tag{14}$$

$$\begin{aligned} r^x_{\rm o1} &= \frac{1}{r_{\rm o1}}\left[\frac{\sqrt{3}}{2}\cos(\phi)+\frac{1}{2}\sin(\phi)\right]^2,\\ r^y_{\rm o1} &= \frac{1}{r_{\rm o1}}\left[-\frac{\sqrt{3}}{2}\sin(\phi)+\frac{1}{2}\cos(\phi)\right]^2,\\ r^z_{\rm o1} &= \frac{h^2}{r_{\rm o1}}, \end{aligned} \tag{15}$$

$$\begin{aligned} r^x_{78} &= \frac{1}{r_{78}}\Big[-0.36\cos(\phi)+0.37\sin(\phi)\Big]^2,\\ r^y_{78} &= \frac{1}{r_{78}}\Big[0.36\sin(\phi)+0.37\cos(\phi)\Big]^2,\\ r^z_{78} &= 0, \end{aligned} \tag{16}$$

$$\begin{aligned} r^x_{15} &= \frac{1}{r_{15}}\Big[0.37\sin(\phi)\Big]^2,\\ r^y_{15} &= \frac{1}{r_{15}}\Big[0.37\cos(\phi)\Big]^2,\\ r^z_{15} &= 0. \end{aligned} \tag{17}$$

By entering these coefficients in (9)–(11) and using (8), the effect of strain on electronic properties can be investigated.

4.2. Stability of penta-graphene nanoribbon

To study the effect of uniaxial strain along the periodic direction of nanoribbon on the stability of nanoribbon, the stress–strain curve was investigated for all three configurations using the density functional theory (DFT) implemented in Quantum ESPRESSO code. Different values of strain were applied to the structure, and then force relaxation calculation was done to reach the most stable structure at any applied strain. The generalized gradient approximation presented by Perdew–Burke–Ernzerhof (GGA-PBE) was used to include the exchange-correlation effect between valence electrons. The basis set function of electrons is expanded by the plane wave method. A 60 Ry energy cut-off to the wave function is selected to expand the wave function Fourier series terms. Also, using the Monkhorst–Pack scheme, k-sampling integration in the whole of the first Brillouin zone was performed. The optimized value of k-mesh was $12 \times 1 \times 1$ to force relaxation calculation.

The uniaxial mechanical strain was applied along the periodic direction ($\phi = 0$) of the considered nanoribbons to control the electronic properties. First, it was necessary to investigate the structural stability of the systems under mechanical strain (see Fig. 4). The results show that structural stability is preserved up to 10% strain for BB and ZB nanoribbons, while structural deformation occurs at approximately 16% strain for the ZZ configuration. This difference is due to the effect of dangling bonds at the edge of the nanoribbons, as the dangling bond effect is more remarkable for the BB and ZB systems compared to the ZZ configuration. Hence,

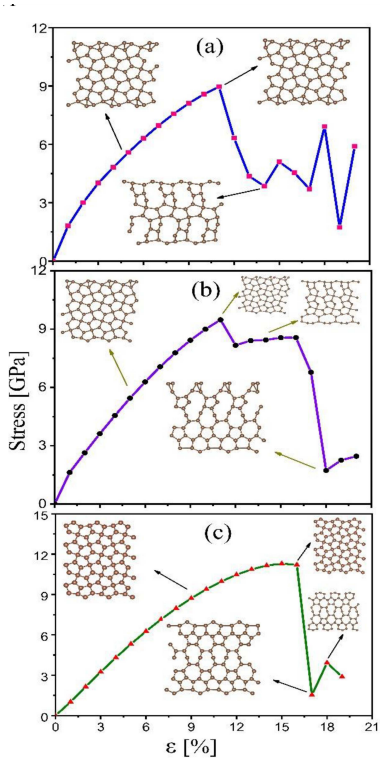

Fig. 4. Strain versus stress curves of considered nanoribbons for: (a) BB, (b) ZB, and (c) ZZ configurations. Inset figures illustrate the crystal structure at different strain value.

edge reconstruction is more significant for the BB and ZB systems. As a result, the ZZ configuration was more stable than the other nanoribbons. Unlike other tight-binding research works, we did not apply arbitrary amounts of strain to the structure. First, the strain was calculated in terms of the stress using DFT. Then, for the structure to be stable, as shown in Fig. 4, the allowable amounts of strain were applied. In allowable amounts of strain, the structure remains stable and does not deform under the application of these values.

The structural response of a material is closely related to its performance in various applications, including mechanical, electrical, and optical properties. Recent studies have demonstrated that penta-graphene nanoribbons are highly stable and exhibit excellent mechanical properties. They have a high Young's modulus and negative Poisson's ratio, making them ideal for use in structural applications where strength and stiffness are essential. Regarding their optical properties, penta-graphene nanoribbons have been shown to exhibit unique electronic and optical properties due to their unique structure. They have a narrow bandgap, which makes them suitable for use in electronic devices such as transistors and sensors. However, penta-graphene nanoribbons passivated with other X atoms (= N, P, O, S, and H) are more stable than their pristine state. Although the total energy calculations indicate the metastability of PG as compared to graphene, it is still found more stable than some successfully synthesized structures, i.e., T-carbon, C20, and cyclocarbon sheet, etc. Zhang et al. [67] have also shown that although increasing temperature reduces failure stress, H-PG? still offers about 71–88% higher values than that of the pristine PG. Generally, research shows that PGNR is meta-stable compared to the armchair and zigzag graphene nanoribbons, but it is energetically more stable than the well-established armchair α-graphyne nanoribbons. So, relying on the computational methods, it is highly convincing that PGNR is energetically as well as dynamically stable (see [46, 54, 68–70]).

5. Results and discussion

5.1. Electronic properties of penta-graphene nanoribbon

First, we computed the band structure of penta-graphene using TBA. In addition, the dependence of PGNR bandgaps on uniaxial strain and ribbon width was investigated (see Figs. 5 and 6). The values of the uniaxial strain in the x-direction were assumed to be 0.05, 0.10, and 0.15. The computed electronic band structures of PGNR for the ZB, ZZ, and BB geometries are shown in Fig. 5. It was found that the calculated bandgaps of the pristine (without strain) PGNR for the three geometries ZB, ZZ, and BB were 0.32, 1.05, and 1.01 eV, respectively. Hence, penta-graphene nanoribbons are direct bandgap semiconductors.

The presence of a direct gap in the electronic properties of penta-graphene nanoribbons has significant implications. Firstly, it indicates that the relatively small energy difference between the top of the valence band and the bottom of the conduction band allows efficient electron transitions [71]. In contrast, materials with an indirect gap require additional momentum transfer for electron transitions, making them less efficient [72]. Secondly, a direct gap suggests that the absorption and emission of light by penta-graphene nanoribbons will be more efficient. Direct bandgap materials can absorb and emit photons with energies close to the bandgap energy and may be better suited for optical devices [73]. Additionally, the presence of a direct gap implies that PGNRs may exhibit enhanced charge carrier mobility. However, the emergence of a direct gap in PGNR indicates improved efficiency in electron transitions, enhanced optical properties, and potentially higher charge carrier mobility.

It can be clearly seen that edge deformation leads to a significant variation in band structures with semiconductor properties. From the evaluated electronic band structures, we find that the magnitude of the bandgap in each type of the PG nanoribbon decreased as the applied strain increased (see Fig. 5). The C–C bond length changes with

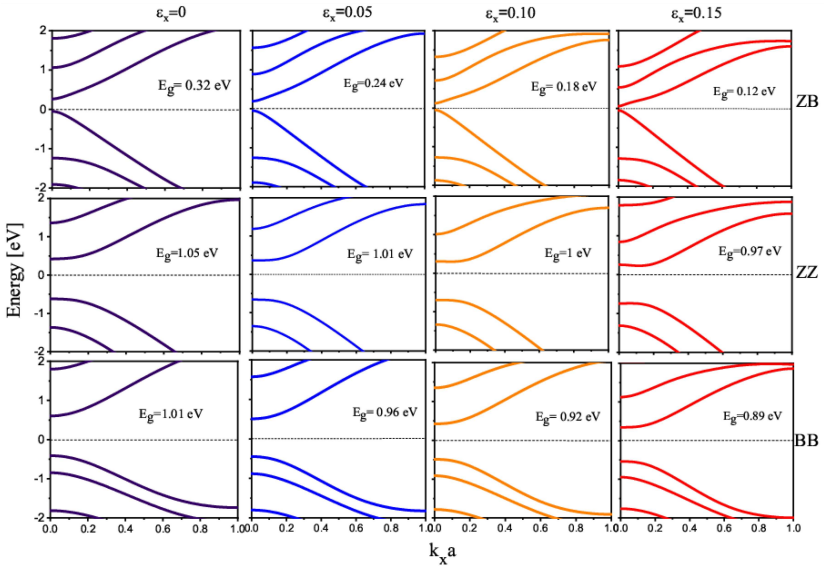

Fig. 5. Electronic band structures of PGNR for the three geometries ZB, ZZ, and BB nanoribbons, while values of uniaxial strain in the x-direction are considered to be 0, 0.05, 0.10, and 0.15. The zero of energy is set to the Fermi level.

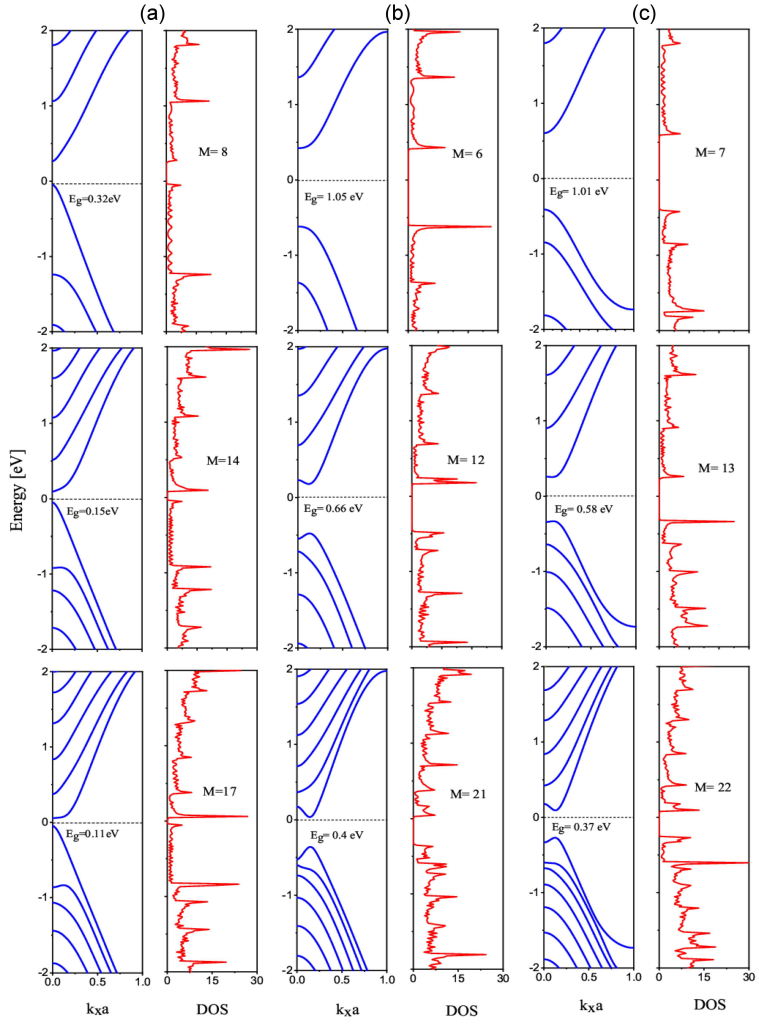

Fig. 6. Dependence of the electrical properties on the PG ribbons width for the three geometries ZB (panel a), ZZ (panel b), and BB (panel c). As can be seen, their band structures are changing and the bandgap decreases with increase of width.

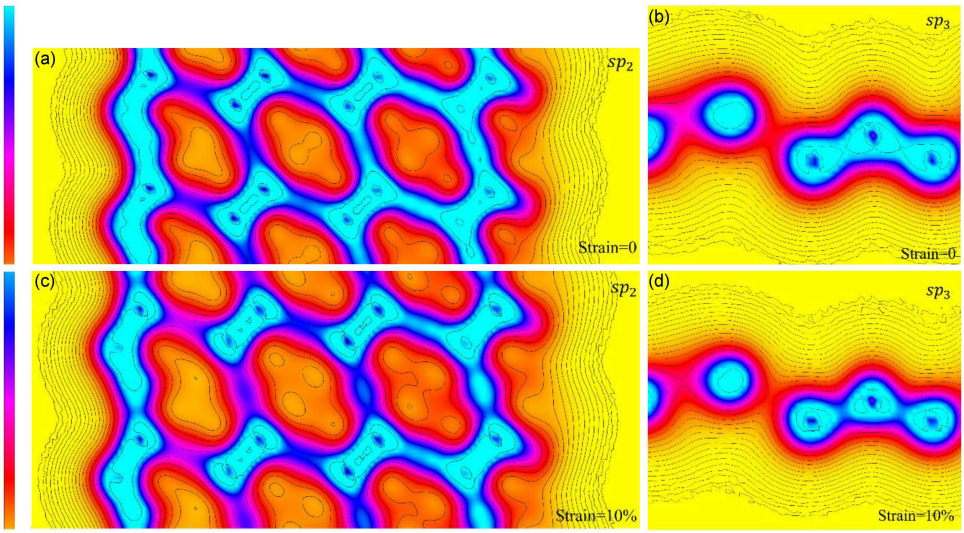

Fig. 7. The charge density distribution of SP_2 and SP_3 hybridized carbon atoms was analyzed using DFT calculations in two states, without and with strain; (a) C_2 (SP_2) atom without strain, (b) C_1 (SP_3) atom without strain, (c) C_2 (SP_2) atom with 10% strain applied, (d) C_1 (SP_3) atom with 10% strain applied. The results show that the SP_3 bond is more vulnerable to failure than the SP_2 bond due to longer bond length and lower charge density.

the tensile strain, and therefore any change in the bond length under the uniaxial strain leads to variation in the overlap of the electron wave functions, and, in turn, to a significant modification of the PGNR bandgap and electronic properties. Stronger double bonds between the hybridized SP_2 atoms (C_2–C_2 bonds) are associated with a greater overlap of carbon atoms, as opposed to the case where the interactions SP_2–SP_3 (or C_1–C_2 bonds) are considered between atoms. Under tensile strain, as the bond length increased, the overlap of the wave functions decreased. Consequently, the influence of the SP_2–SP_2 double bond on the electronic properties becomes stronger. Thus, the application of a strain provides a way to tune the bandgap of PGNR. These semiconducting behaviors are intimately related to the suppression of the edge states of the edge C atoms due to the effects of the termination atoms. Therefore, by modifying the edge and applying strain, the bandgap can be controlled for different purposes.

Distortion of the penta-graphene lattice under strain leads to changes in the bond angles, lengths between carbon atoms, and buckling of the structure. In penta-graphene, SP_2–SP_2 interactions are stronger (because of the C=C double bond) than SP_2–SP_3 interactions. The SP_2–SP_3 hybridized bond is more vulnerable to failure than the SP_2–SP_2 bond due to the longer bond length and lower charge density of SP_3. When strain is applied, the stronger interactions dominate and cause a decay in the energy gap [74].

Materials with a similar two-dimensional carbon lattice, such as graphene or other graphitic materials, may exhibit similar behavior under strain due to their strong SP_2 bonding. Also, other factors, such as lattice symmetry and buckling, can affect the response to strain and electronic properties [75]. In order to further confirm the above statements, we have analyzed the charge density distribution for carbon atoms with different hybridization using the DFT method. For clarity, the results are shown in Fig. 7.

It is noteworthy that gap opening in PGNR is theoretically also achievable by doping [76]. However, this method typically leads to phase transitions (see [76]), so effective control of nanostructure properties becomes difficult. Doping impurity is expensive for our desired structure because we have two types of carbon with different hybridization (SP_2 and SP_3) in penta-graphene. Doping impurity on each of the carbons causes a new behavior, so it is not possible to have quick control of the properties of the material. Also, when an impurity is doped in the structure, a phase transition usually occurs, which is not suitable for our desired applications. Generally, it is important to note that both strain-induced effects and doping strategies have their own unique advantages and limitations, depending on the specific application requirements and material properties.

In Fig. 6, the dependence of the electronic properties on the ribbon width is shown. The associated band structures and density of states of penta-graphene nanoribbons with different widths of $M = 8, 14, 17$, $M = 6, 12, 21$, and $M = 7, 13, 22$, are plotted in Fig. 6 for the ZB, ZZ, and BB geometries, respectively. As can be seen, the band structures change and the bandgap decreases with an increase in width. In fact, when the ribbon width increases, the quantum confinements are reduced, so that the intrinsic mobility of the electric charge

carriers increases and tends gradually to the case of a 2D structure. Our results are consistent with other studies on graphene nanoribbons [77, 78]. Due to the one-dimensional nature of graphene NR (GNR) and PGNR, the bandgaps of nanoribbons arise from quantum confinement and are significantly affected by edges and widths. Broadly speaking, these results suggest that the electronic properties of ribbons can be significantly tuned by modifying the edges through the use of strain and width manipulation. Hence, such configurations of PGNRs are expected to be widely applied in nano-electronic devices.

5.2. Transport properties of penta-graphene nanoribbon

In the following, we investigated transport properties using the TB model and the generalized Green's function method in the Landauer–Buttiker formalism. Many studies have been done using this method, and the transport properties of materials have been investigated. For example, there are studies on the transport properties of SS-pSiC_2 NRs under a sequence of uniaxial strains [79], the electronic transport properties of lateral heterojunctions composed of penta-GNR and penta-B_2N_4 nanoribbons [80], and the transport properties of monolayer PG with typical small gas molecules [81]. Furthermore, recently the transport characteristics of sawtooth penta-graphene nanoribbons have been investigated by Than Tien et al. [82], and the electron transport of a sawtooth penta-graphene nanoribbon (SSPGNR) under uniaxial strains was theoretically studied by Van On et al. [74]. The transport in our work is ballistic because ballistic transport is a nanoscale phenomenon at low temperatures [83–86] and can be engineered in nanodevices. For device systems, the current through the system was calculated using the Landauer–Büttiker formula [84–86]

$$I(V) = \frac{2e}{h}\int_{-\infty}^{\infty} \mathrm{d}E \;\; T(E,V)\Big[f(E-\mu_L)-f(E-\mu_R)\Big]. \tag{18}$$

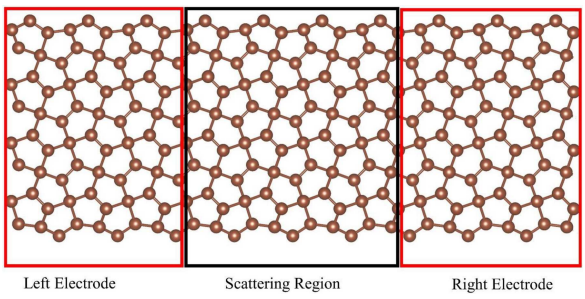

Fig. 8. Schematic illustration of the transport device. All three areas are of the same material.

Here, $f(E-\mu_L)$ and $f(E-\mu_R)$ are Fermi distribution functions with electrochemical potentials in the left and right leads, respectively; $T(E,V)$ is the transmission spectrum of incident electrons at energy E and bias V from the left electrode to the right electrode. The electrochemical potential difference between the two electrodes is $\mu_L-\mu_R$. Indeed, the transmission function indicates the rate at which electrons are transmitted from the left to the right electrode by propagating through the molecule. The transmission spectrum and total conductance are obtained, respectively, from the equations [84–86]

$$T(E,V) = \mathrm{Tr}\Big[\Gamma_L(E,V)\; G(E,V)\; \Gamma_R\; G^{\dagger}(E,V)\Big] \tag{19}$$

and

$$G = \frac{2e}{h}\; T(E,V). \tag{20}$$

In (19)–(20), G and $G^{\dagger}$ are the advanced and retarded Green functions of the scattering region, respectively, while Γ_R and Γ_L are the coupling functions from the right and left electrodes, respectively. The Green function of the system based on the Hamiltonian of the central (scattering) region (H_C) can be written as

$$G = \Big[(E+\mathrm{i}\eta)\,\hat{\mathbb{I}} - H_C - \Sigma_R - \Sigma_L\Big]^{-1}, \tag{21}$$

and the coupling functions Γ_R and Γ_L can be calculated through the expression

$$\Gamma_{R(L)} = \mathrm{i}\big[\Sigma_{R(L)} - \Sigma^{\dagger}_{R(L)}\big]. \tag{22}$$

Here, $\Sigma_R = H_{Rc}G_R H^{\dagger}_{Rc}$ and $\Sigma_L = H^{\dagger}_{Lc}G_L H_{Lc}$ are the self-energy terms from the two electrodes; H_{Rc} and H_{Lc} are the Hamiltonians related to the interaction of the right and left electrodes with the scattering region and they will be non-zero only for the adjacent points in the scattering region; $G_R = [(E+\mathrm{i}\eta)\,\hat{\mathbb{I}} - H_{Rc}]^{-1}$ and $G_L = [(E+\mathrm{i}\eta)\,\hat{\mathbb{I}} - H_{Lc}]^{-1}$ correspond to Green's functions for the right and left electrodes, respectively; E is the injecting energy of the source electron; $\hat{\mathbb{I}}$ is a unitary matrix in Hamiltonian dimensions; and η is a very small number. Therefore, by calculating the self-energies, the coupling functions Γ_R and Γ_L can be easily obtained, and then the transmission spectrum will be obtained from the expression given as (19).

In addition, the quantity $G_0 = \frac{2e}{h}$ — called the conductance quantum — is a natural unit for conductance measurements in mesoscopic systems. A schematic of the transport device based on PGNR is shown in Fig. 8. In this device, three regions (semi-infinite left electrode, central scattering region, and semi-infinite right electrode) are of the same material (PGNR).

Figures 9 and 10 show the I–V and T–E curves of ZB, ZZ, and BB type PGNR structures under tensile strains ε_x and with different widths of M. Thus, by tuning the width of PGNRs and applying strain, we can achieve the maximum current and

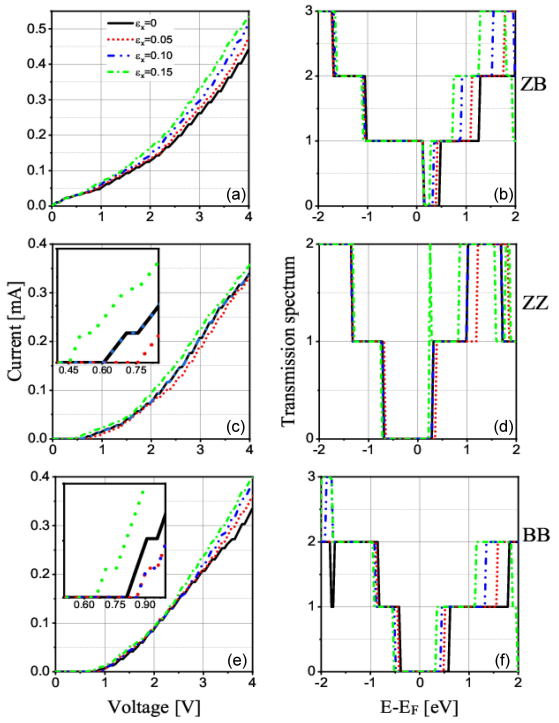

Fig. 9. The I–V curves (a, c, e) and transmission spectrum (b, d, f) under various uniaxial strain values. The threshold voltage values of ZZ and BB configurations are shown in the insets of (c, e) panels.

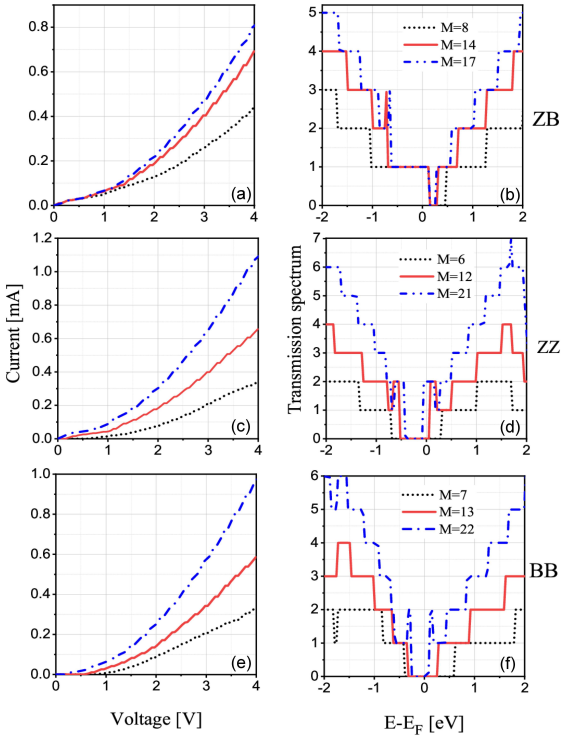

Fig. 10. The I–V curves (a, c, e) and transmission spectrum (b, d, f) with different widths. As the width of the nanoribbon is increased, the current intensity and threshold voltage are increased and decreased, respectively.

lower threshold voltage (see Fig. 9). As shown in Fig. 9, the threshold voltage of the ZB configuration is zero. For both ZZ and BB configurations, the lowest threshold voltage value is obtained at a strain value of 0.15. Specifically, the threshold voltage values are 0.45 V and 0.65 V for the ZZ and BB configurations, respectively. Consequently, applied strain allows lower threshold voltage values to be achieved. Figure 10 shows the I–V curves and conductance as a function of the injected electron energy with different widths and in the absence of strain. With an increase in the width of the nanoribbon, the current intensity increased in the voltage range of 0.0–4.0 V. Among the three mentioned configurations, ZZ has the highest electric conductance and electric current for a width of $M = 21$ atoms. In fact, with an increase in the width of the nanoribbon, the available energy levels increase, the highest valence band and the lowest conduction band are closer to the Fermi level, electron transfer becomes easier, and more electrons move from the left to the right side. This can be observed in the electrical conductance diagrams. As shown in the graphs of the density of states and electrical conductance, in the energy gap ranges, the electrical conductance has no value. In addition, the magnitude of the current in the pristine penta-graphene ZZ model was maximized at higher voltages and widths. The behavior of the computed transmission spectrum is in agreement with the I–V characteristics.

6. Conclusions

In summary, by examining the electronic and transport properties of the three configurations of PGNR by tight-binding model (TBA), we found that all three geometries are direct bandgap semiconductors. Unlike other tight-binding studies, we did not apply arbitrary amounts of strain to the structure. First, the strain was calculated in terms of stress using DFT. For the structure to be stable and not deformed, allowed amounts of strain were applied. Based on the TBA model, we found that the magnitude of the bandgap in each type of PGNR is reduced as the applied strain increases. In addition, for the three geometries, the band structures change and the bandgap decreases with increasing width. Hence, such configurations of PGNRs are expected to be widely used in nano-electronic devices. Finally, we investigated transport properties using a tight-binding model and a generalized Green's function method in the Landauer–Buttiker formalism. Thus, by tuning the width of PGNRs and applying strain, we achieved the maximum current and lower threshold voltage. Also, as the width of the nanoribbon increases, the intensity of the current increases, and the available energy levels increase. Moreover, the results show that the magnitude of the current in the pristine penta-graphene ZZ model is maximized at

higher voltages and widths. The behavior of the computed transmission spectrum is in agreement with the I–V characteristics. Our calculations may suggest its potential applications in spin electronics, nano-electronic devices, and solar cells, which also provide some theoretical guidance for regulating the properties of PGNR by applying strain, edge modifications, and different widths. In general, our study opens a way to design and fabricate pentagraphene-based electronic devices.

References

[1] A.H. Castro Neto, F. Guinea, N.M. Peres, K.S. Novoselov, A.K. Geim, *Rev. Mod. Phys.* **81**, 109 (2009).

[2] R.R. Nair, P. Blake, A.N. Grigorenko, K.S. Novoselov, T.J. Booth, T. Stauber, N.M.R Peres, A.K. Geim, *Science* **320**, 1308 (2008).

[3] P. Blake, E.W. Hill, A.H. Castro Neto, K.S. Novoselov, D. Jiang, R. Yang, T.J. Booth, A.K. Geim, *Appl. Phys. Lett.* **91**, 063124 (2007).

[4] F. Bonaccorso, Z. Sun, T. Hasan, A. Ferrari, *Nat. Photon.* **4**, 611 (2010).

[5] W. Choi, N. Choudhary, G.H. Han, J. Park, D. Akinwande, Y.H. Lee, *Mater. Today* **20**, 116 (2017).

[6] R. Dong, I. Kuljanishvili, *J. Vac. Sci. Technol. B* **35**, 030803 (2017).

[7] S. Manzeli, D. Ovchinnikov, D. Pasquier, O.V. Yazyev, A. Kis, *Nat. Rev. Mater.* **2**, 17033 (2017).

[8] A.V. Kolobov, J. Tominaga, *Two-Dimensional Transition-Metal Dichalcogenides* Vol. 239, Springer, 2018.

[9] C. Pan, Y. Ji, N. Xiao et al., *Adv. Funct. Mater.* **27**, 1604811 (2017).

[10] A.J. Mannix, X.F. Zhou, B. Kiraly et al., *Science* **350**, 1513 (2015).

[11] B. Feng, J. Zhang, Q. Zhong et al., *Nat. Chem.* **8**, 563 (2016).

[12] W. Li, L. Kong, C. Chen et al., *Sci. Bull.* **63**, 282 (2018).

[13] P. Vogt, P. De Padova, C. Quaresima, J. Avila, E. Frantzeskakis, M.C. Asensio, A. Resta, B. Ealet, G. Le Lay, *Phys. Rev. Lett.* **108**, 155501 (2012).

[14] C.L. Lin, R. Arafune, K. Kawahara, N. Tsukahara, E. Minamitani, Y. Kim, N. Takagi, M. Kawai, *Appl. Phys. Express* **5**, 045802 (2012).

[15] J.L. Zhang, S. Zhao, C. Han et al., *Nano Lett.* **16**, 4903 (2016).

[16] J.P. Xu, J.Q. Zhang, H. Tian, H. Xu, W. Ho, M. Xie, *Phys. Rev. Mater.* **1**, 061002 (2017).

[17] J. Zhuang, C. Liu, Q. Gao et al., *ACS Nano* **12**, 5059 (2018).

[18] M. Naguib, O. Mashtalir, J. Carle, V. Presser, J. Lu, L. Hultman, Y. Gogotsi, M.W. Barsoum, *ACS Nano* **6**, 1322 (2012).

[19] M. Naguib, M. Kurtoglu, V. Presser et al., *Adv. Mater.* **23**, 4248 (2011).

[20] R. Xu, X. Zou, B. Liu, H.M. Cheng, *Mater. Today* **21**, 391 (2018).

[21] J.M. Pontes, N. Frazão, D.L. Azevedo, J.R. Lima, *Comput. Mater. Sci.* **188**, 110210 (2021).

[22] S. Zhang, J. Zhou, Q. Wang, X. Chen, Y. Kawazoe, *Proc. Natl. Acad. Sci. USA* **112**, 2372 (2015).

[23] H. Einollahzadeh, S.M. Fazeli, R.S. Dariani, *Sci. Technol. Adv.* **17**, 610 (2016).

[24] A.D. Oyedele, S. Yang, L. Liang et al., *J. Am. Chem. Soc.* **139,** 14090 (2017).

[25] W.L. Chow, P. Yu, F. Liu et al., *Adv. Mater.* **29**, 1602969 (2017).

[26] E. Li, D. Wang, P. Fan et al., *Nano Res.* **11**, 5858 (2018).

[27] J. Li, X. Fan, Y. Wei, G. Chen, *Sci. Rep.* **6**, 31840 (2016).

[28] Z. Liu, H. Wang, J. Sun, R. Sun, Z.F. Wang, J. Yang, *Nanoscale* **10**, 16169 (2018).

[29] M. Yagmurcukardes, H. Sahin, J. Kang, E. Torun, F.M. Peeters, R.T. Senger, *J. Appl. Phys.* **118**, 104303 (2015).

[30] G.R. Berdiyorov, M.E.A. Madjet, *RSC Adv.* **6**, 50867 (2016).

[31] S. Zhang, J. Zhou, Q. Wang, P.J. Jena, *Phys. Chem. C* **120**, 3993 (2016).

[32] T. Zhao, S. Zhang, Y. Guo, Q. Wang, *Nanoscale* **8**, 233 (2016).

[33] J.I. Cerda, J. Slawinska, G. Le Lay, A.C. Marele, J.M. Gomez Rodriguez, M.E. Davila, *Nat. Commun.* **7**, 13076 (2016).

[34] Y. Guo, C. Zhang, J. Zhou, Q. Wang, P. Jena, *Phys. Rev. Appl.* **11**, 064063 (2019).

[35] R. Krishnan, W.S. Su, H.T. Chen, *Carbon* **114**, 465 (2017).

[36] R. Krishnan, S.Y. Wu, H.T. Chen, *Carbon* **132**, 257 (2018).

[37] N. Sathishkumar, S.Y. Wu, H.T. Chen, *Int. J. Energy Res.* **43**, 4867 (2019).

[38] N. Sathishkumar, S.Y. Wu, H.T. Chen, *Chem. Eng. J.* **391**, 123577 (2020).

[39] E. Ressouche, V. Simonet, B. Canals, M. Gospodinov, V. Skumryev, *Phys. Rev. Lett.* **103**, 267204 (2009.

[40] Y.Y. Zhang, Q.X. Pei, Y. Cheng, Y.W. Zhang, X. Zhang, *Comput. Mater. Sci.* **137**, 195 (2017).

[41] H. Liu, G. Qin, Y. Lin, M. Hu, *Nano Lett.* **16**, 3831 (2016).

[42] F.Q. Wang, J. Yu, Q. Wang, Y. Kawazoe, P. Jena, *Carbon.* **105**, 424 (2016).

[43] H. Sun, S. Mukherjee, C.V. Singh, *Phys. Chem. Chem. Phys.* **18**, 26736 (2016).

[44] W. Xu, G. Zhang, B. Li, *J. Chem. Phys.* **143**, 154703 (2015).

[45] A.A. Balandin, *Nat. Mater.* **10**, 569 (2011).

[46] B. Rajbanshi, S. Sarkar, B. Mandal, P. Sarkar, *Carbon* **100**, 118 (2016).

[47] H. Qin, Ch. Feng, X. Luan, D. Yang, *Nanoscale Res. Lett.* **13**, 1 (2018).

[48] F. Miao, S.J. Liang, B. Cheng, *npj Quant. Mater.* **6**, 59 (2021).

[49] H. Duan, S. Li, S.H. Zheng, Z. Sun, M. Yang, R.Q. Wang, *New J. Phys.* **19**, 103010 (2017).

[50] V.M. Pereira, A.H. Castro Neto, *Phys. Rev. Lett.* **103**, 046801 (2009).

[51] F. Bloch, *Z. Phys.* **52**, 555 (1929).

[52] M. Nakhaee, S.A. Ketabi, F.M. Peeters, *Comput. Phys. Commun.* **254**, 107379 (2020).

[53] S. Boker, M. Neale, H. Maes et al., *Psychometrika* **76**, 306 (2011).

[54] S. Zhang, J. Zhou, Q. Wang, X. Chen, Y. Kawazoe, P. Jena, *Proc. Natl. Acad. Sci. USA* **112**, 2372 (2015).

[55] Y. Zhao, X. Li, J. Liu, C. Zhang, Q. Wang, *J. Phys. Chem. Lett.* **9**, 1815 (2018).

[56] K. Dolui, S. Quek, *Sci. Rep.* **5**, 11699 (2015).

[57] L.L. Li, D. Moldovan, W. Xu, F.M. Peeters, *Phys. Rev. B.* **96**, 155425 (2017).

[58] M. Zare, *Mater. Res. Express* **6**, 105097 (2019).

[59] S. Datta, *Quantum Transport: Atom to Transistor*, Cambridge University Press, 2005.

[60] M. Zare, *J. Appl. Phys.* **128**, 163903 (2020).

[61] F. Afshari, M. Ghaffarian, *Physica E* **89**, 86 (2017).

[62] A.N. Rudenko, M.I. Katsnelson, *Phys. Rev. B* **89**, 201408(R) (2014).

[63] W.A. Harrison, *Elementary Electronic Structure*, World Scientific, 1999.

[64] H. Tang, J.W. Jiang, B.S. Wang, Z.B. Su, *Solid State Commun.* **149**, 82 (2009).

[65] J.W. Jiang, S.P. Harold, *Phys. Rev. B* **91**, 235118 (2015).

[66] P. Liu, X. Zhou, X. Xiao, B. Zhou, G. Zhou, *J. Phys. Condens. Matter.* **32**, 285301 (2020).

[67] Y. Zhang, Q. Pei, Z. Sha, Y. Zhang, H. Gao, *Nano Res.* **10**, 3865 (2017).

[68] T. Wu, M. Yao, J. Li, M. Li, M. Long, *Results Phys.* **17**, 103103 (2020).

[69] M.A. Nazir, A. Hassan, Y. Shen, Q. Wang, *Nano Today* **44**, 101501 (2022).

[70] L. Wang, Y. Chen, H. Miura, K. Suzuki, C. Wang, *J. Phys. Condens. Matter* **34**, 505301 (2022).

[71] P. Zhang, V.H. Crespi, E. Chang, S.G. Louie, M.L. Cohen, *Nature* **409**, 69 (2001).

[72] P.D. Sreedevi, R. Vidya, P. Ravindran, *Sol. Energy* **190** 350 (2019).

[73] V.B. Pawade, Sanjay J. Dhoble, H.C. Swart, *Nanoscale Compound Semiconductors and Their Optoelectronics Applications*, Woodhead Publishing series, Elsevier, 2022.

[74] V. Van On, L.N. Thanh, N.T. Tien, *Phil. Mag.* **100**, 1834 (2020).

[75] H. Alborznia, M. Naseri, N. Fatahi, *Superlattices Microstruct.* **133**, 106217 (2019).

[76] R.M. Santos, L.E. Sousa, D.S. Galvão, L.A. Ribeiro, *Sci. Rep.* **10**, 8014 (2020).

[77] Y.W. Son, M.L. Cohen, S.G. Louie, *Phys. Rev. Lett.* **97**, 216803 (2006).

[78] L. Yang, C.H. Park, Y.W. Son, M.L. Cohen, S.G. Louie, *Phys. Rev. Lett.* **99**, 186801 (2007).

[79] V.V. On, P.T.B. Thao, L.N. Thanh, N.T. Tien, *AIP Adv.* **12**, 095318 (2022).

[80] X. Yi, M. Long, A. Liu, S. Zhang, M. Li, H. Xu, *Physica B* **595**, 412362 (2020).

[81] M.Q. Cheng, Q. Chen, K. Yang, W.Q. Huang, W.Y. Hu, G.F. Huang, *Nanoscale Res. Lett.* **14**, 306 (2019).

[82] N.T. Tien, P.T.B. Thao, V.T. Phuc, R. Ahuja, *Physica E* **114**, 113572 (2019).

[83] S. Weingart, C. Bock, U. Kunze, F. Speck, T. Seyller, L. Ley, *Appl. Phys. Lett.* **95**, 262101 (2009).

[84] M. Büttiker, Y. Imry, R. Landauer, S. Pinhas, *Phys. Rev. B* **31**, 6207 (1985).

[85] R. Landauer, *IBM J. Res. Dev.* **1**, 223 (1957).

[86] S. Datta, *Electronic Transport in Mesoscopic Systems*, Cambridge University Press, 1997.